batteries

MDPI

Article

The Impact of Structural Pattern Types on the Electrochemical Performance of Ultra-Thick NMC 622 Electrodes for Lithium-Ion Batteries

Penghui Zhu *, Benjamin Ebert, Peter Smyrek and Wilhelm Pfleging

Institute for Applied Materials-Applied Material Physics (IAM-AWP), Karlsruhe Institute of Technology (KIT), Hermann-von-Helmholtz-Platz 1, 76344 Eggenstein-Leopoldshafen, Germany; benni-ebert@gmx.de (B.E.); peter.smyrek@gmx.de (P.S.); wilhelm.pfleging@kit.edu (W.P.)
* Correspondence: penghui.zhu@kit.edu

Abstract: An increase in the energy density on the cell level while maintaining a high power density can be realized by combining thick-film electrodes and the 3D battery concept. The effect of laser structuring using different pattern types on the electrochemical performance was studied. For this purpose, $LiNi_{0.6}Mn_{0.2}Co_{0.2}O_2$ (NMC 622) thick-film cathodes were prepared with a PVDF binder and were afterward structured using ultrafast laser ablation. Eight different pattern types were realized, which are lines, grids, holes, hexagonal structures, and their respective combinations. In addition, the mass loss caused by laser ablation was kept the same regardless of the pattern type. The laser-structured electrodes were assembled in coin cells and subsequently electrochemically characterized. It was found that when discharging the cells for durations of less than 2 h, a significant, positive impact of laser patterning on the electrochemical cell performance was observed. For example, when discharging was performed for one hour, cells containing laser-patterned electrodes with different structure types exhibited a specific capacity increase of up to 70 mAh/g in contrast to the reference ones. Although cells with a hole-patterned electrode exhibited a minimum capacity increase in the rate capability analysis, the combination of holes with lines, grids, or hexagons led to further capacity increases. In addition, long-term cycle analyses demonstrated the benefits of laser patterning on the cell lifetime, while cyclic voltammetry highlighted an increase in the Li-ion diffusion kinetics in cells containing hexagonal-patterned electrodes.

Keywords: laser ablation; lithium-ion battery; 3D battery; NMC 622 cathodes; ultra-thick electrodes; rate capability; lifetime

Citation: Zhu, P.; Ebert, B.; Smyrek, P.; Pfleging, W. The Impact of Structural Pattern Types on the Electrochemical Performance of Ultra-Thick NMC 622 Electrodes for Lithium-Ion Batteries. *Batteries* **2024**, *10*, 58. https://doi.org/10.3390/batteries10020058

Academic Editor: Alejandro Varez

Received: 25 December 2023
Revised: 29 January 2024
Accepted: 5 February 2024
Published: 8 February 2024

1. Introduction

Lithium-ion batteries (LIBs) have been developed rapidly since their first commercialization more than 30 years ago and are taking over market due to their high energy density as well as high power density in contrast to lead-acid, Ni-metal hydride (NiMH), and Na-/K-ion batteries [1,2]. The specific energy (Wh/kg) of LIBs with a cylindrical cell design is continuing to increase by about 6% per year [3]. However, this still does not fulfil the need for an increased electric mobility. In addition, fast charging and the energy density of batteries are still limiting factors for battery electric vehicles (BEVs).

A high power density can be achieved by using thin-film electrodes, whereas the energy density at the cell level may be significantly reduced due to the high ratio of inactive components/active components inside the battery. To increase the energy density of a battery at the material level, electrode materials with a high specific energy density can be applied, while at the cell level, a high energy density can be achieved by adapting thick-film electrodes. In addition, using less inactive material leads to a material-related cost reduction [4]. However, increasing the electrode film thickness could lead to technical issues during manufacturing, such as peeling of electrodes and crack formation during drying

and rewinding [5]. In addition, a serious capacity drop and a significant resistance increase might take place during cycling at elevated electrical currents due to the accumulation of cell polarization and local material degradation [5,6].

The three-dimensional (3D) battery concept was introduced for micro-batteries by Long et al. [7] in order to counteract the trade-off between energy and power density while maintaining a short Li-ion transport distance between electrodes. Extrusion-based printing [8,9], direct ink writing (DIW) [10,11], micro-casting using patterned blades [12], mechanical embossing [13], and template-based manufacturing [14–16] were reported to be able to create cathodes with 3D architectures. However, most of these techniques are not efficient or entail extreme conditions pre- or post-processing; thus, they may not be suitable for mass production in the battery industry.

Laser ablation can be applied to achieve 3D architectures in electrodes for LIBs. This innovative processing technique was introduced for composite electrodes about 12 years ago by Pröll et al. [17]. Compared to conventional patterning techniques, laser processing has many advantages, such as non-contact characteristics, a high precision, and flexible processing, and it requires no subsequent processing steps. In addition, with line structures, the wetting of the liquid electrolyte in laser-patterned electrodes can be accelerated due to capillary forces [18–20]. In addition, an enhanced capacity retention at high discharge/charge rates and a reduced charge transfer resistance were observed in cells containing laser-patterned $Li(Ni_{0.5}Mn_{0.3}Co_{0.2})O_2$ (NMC 532) [21], $Li(Ni_{0.6}Mn_{0.2}Co_{0.2})O_2$ (NMC 622) [22–24], $LiCoO_2$ (LCO) [25], $Li(Ni_{0.8}Mn_{0.1}Co_{0.1})O_2$ (NMC 811) [26,27], $LiFePO_4$ (LFP) [28], graphite [23,25,29], and Si/graphite (see reference [30] and those cited therein) using line patterns with varying pitches. In addition, alternative patterns such as through-holes in LFP cathodes [31–33], blind holes in graphite [34–39], and grid patterns in Si/graphite anodes [40] have also been reported. In general, the discharge capacity is enhanced for cells with laser-structured electrodes in contrast to those with unstructured electrodes when they are discharged for less than 2 h. However, the electrode material, mass loading, and pattern type influence the capacity increase. The enhancement occurs at lower applied currents with an increased mass loading.

So far, there have been no studies that compare the impact of different laser-generated patterns on the electrochemical performance at the cell level. Therefore, in this work, different laser-generated patterns were established in NMC 622 cathodes in order to evaluate the electrochemical impact on the cell level. In addition, the processing efficiency was investigated using lines, grids, holes, hexagonal structures, and their combinations. In addition, since the cost of the cathode material accounts for half of the total material cost in LIBs [41], the mass loss was low. Furthermore, it was essential for the comparative study to ensure that the laser-structured cathodes had the same mass loss independently from the applied pattern types. Thus, the pitch of the line structures, the distance between holes, and the side length of the hexagons were adjusted accordingly to maintain a similar mass loss due to laser ablation. After laser structuring, the electrodes were assembled with Li in coin cells (half cells). Rate capability analyses, long-term cycle analyses, and cyclic voltammetry were performed to characterize the electrochemical performance of the cells containing laser-structured NMC 622 electrodes with different pattern types.

2. Materials and Methods

For the slurry preparation, a polycrystalline NMC 622 powder (BASF SE, Ludwigshafen, Germany) with a particle size D90 of 12.8 µm was used, while polyvinylidene fluoride (PVDF) Solef® 5130 (Solvay Specialty Polymers, Brussels, Belgium) was applied as a binder and was dissolved in N-Methyl-2-pyrrolidone (NMP, Merck KGaA, Darmstadt, Germany) solvent with a weight ratio of 1:10 prior to the mixing process. C-NERGY Super C65 carbon black (Imerys G & C Belgium, Willebroek, Belgium) was used as a conductive agent, while KS6L graphite (Imerys G & C Swizerland Ltd., Bodio, Switzerland) was adopted as a compaction aid. The slurry was homogenized using a laboratory dissolver (VD-10 XP, DISTECH GmbH, Kirchen, Germany). The NMC 622 powder and conductive agent

were premixed and added to the PVDF solution in two steps: The first half of the powder was added into the solution and was homogenized at 2000 rpm for 30 min, then extra NMP solvent was added to adjust the slurry solid content to 66.7 wt%. Subsequently, the other half of the powder was added and mixed at 2000 rpm for 50 min without a vacuum and then for 10 min with a vacuum. The container was cooled to 20 °C with water during the entire mixing process. An active material percent of 92 wt% was applied for the slurry preparation, and the weight percent of the other components remained the same as described in our previous work [42].

The obtained slurry was tape-cast with a doctor blade (ZUA 2000.100, Proceq, Schwerzenbach, Switzerland) onto an Al-foil (MTI Corporation, Richmond, CA, USA) with a thickness of 15 µm using a roll-to-roll (R2R) laboratory coater (TMAX-JCT-150, Xiamen Battery Equipments Ltd., Xiamen, China). The coating speed was 5.6 mm/s, and the temperature in the drying chamber was set to 100 °C. In order to achieve electrodes with a high mass loading, the dual-layer coating technique was applied; i.e., a doctor blade height of 250 µm was used for the first coating, and the electrodes were dried and rewound. Afterward, the second coating was set on the top of the first one with a doctor blade height of 345 µm. After drying, the coated electrode films were calendered using an electric precision rolling press (MSK-2150, MTI Corporation, Richmond, CA, USA) at room temperature with a constant calendering speed of 35 mm/s. The porosity of the NMC 622 cathodes was reduced to around 35% and was determined by measuring the electrode thickness and weight, see reference [22] and those cited therein.

The calendered electrodes were afterward patterned using a pulsed fiber laser (FX600, Edgewave GmbH, Würselen, Germany) with a wavelength of 1030 nm, a beam quality of $M^2 < 1.1$, and a laser pulse duration of 600 fs, which was assembled in a laser micromachining system MSV203 (M-Solv Ltd., Oxford, UK). An intelliSCAN III 20 scan head (Scanlab GmbH, Puchheim, Germany) was equipped with an F-Theta lens (Jenoptik AG, Jena, Germany) for laser beam deflection. Eight different structure types were chosen for the laser patterning of ultra-thick-film electrodes, as shown in Figure 1. The basic pattern elements were lines, holes, grids, and hexagons. L1 and L2 were both line structures but with different full widths at half maximum (FWHMs), which were achieved by adjusting the respective laser parameters. For the laser-assisted generation of wider line structures in L2, LiHo, and GHo, a higher line energy ("average laser power" divided by "laser scan speed") was applied compared to that for the L1 pattern.

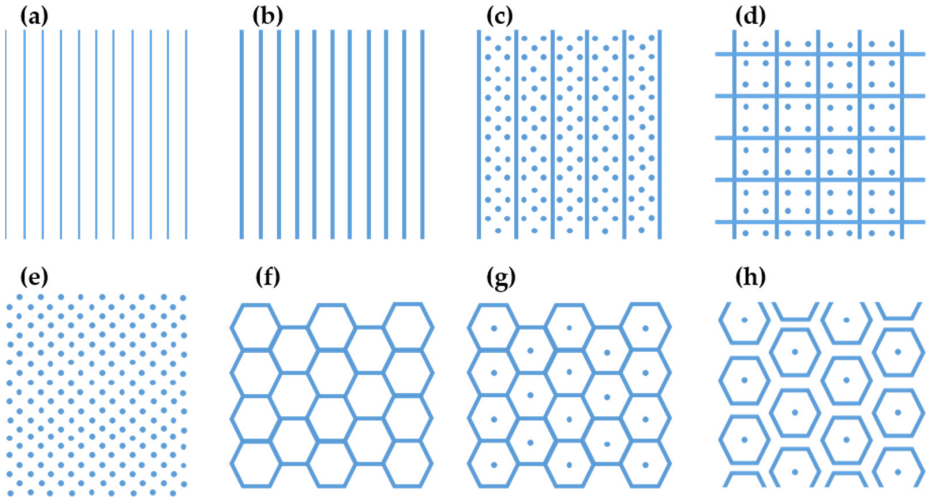

Figure 1. Overview of the different applied pattern types for NMC 622 electrodes: (**a**) narrow (L1) and (**b**) broad (L2) line structures, (**c**) lines combined with holes (LiHo), (**d**) grid structure combined with four square-ranged holes in each grid (GHo), (**e**) triangularly arranged holes (Ho), (**f**) hexagonal structure (Hex), (**g**) the same hexagonal structure but with holes in the center of each hexagon (HexHo), and (**h**) separated hexagonal structure with central holes (Sep.HexHo).

The laser parameters applied for different structures are listed in Table 1. Scanning electron microscopy (SEM, Phenom XL G2 Desktop, Thermo Fisher Scientific Inc., Schwerte, Germany) and cross-sectional analyses were conducted to determine the suitable laser parameters. For the laser patterning of electrodes with line or grid structures, the electrode materials were laser ablated until the current collector was exposed, without affecting the current collector. As for the hole structure, the pitch was set by adjusting the laser repetition rate and laser scanning speed. All laser patterning processes were performed in ambient air.

Table 1. Laser parameters applied to achieve different pattern types in thick-film NMC 622 electrodes.

Pattern Type	Average Laser Power (W)	Laser Repetition Rate (kHz)	Laser Scanning Speed (m/s)	Number of Scan Passes	Line Energy (J/m)
Narrow lines (L1)	46	1500	20	61	2.3
Broad lines (L2) Broad lines + holes (LiHo) Grids + holes (GHo)	73	1500	10	25	7.3
Holes (Ho)	86	100	10	70	-
Hexagons (Hex) Hexagons + holes (HexHo) Separated hexagons + holes (Sep.HexHo)	35	1500	5	18	7.0

For coin cell assembly, the reference NMC 622 cathodes and the laser-patterned cathodes were cut into circles of 12 mm in diameter using an average laser power of 27 W, a repetition rate of 1 MHz, and a laser scanning speed of 5 m/s. All electrodes were dried at 130 °C for 12 h in a vacuum oven (VT 6025, Thermo Fisher Scientific Inc., Schwerte, Germany) prior to cell assembly in order to eliminate the water in the electrodes. Afterward, the electrodes were transferred to a glove box (LAB master pro sp, M. Braun Inertgas-Systeme GmbH, Munich, Germany) filled with argon and were assembled with Li-foil (Merck KGaA, Darmstadt, Germany) with a thickness of 250 µm and a diameter of 16 mm using a CR2032 coin cell format. A polypropylene (PP) separator sheet (Celgard 2500, Charlotte, NC, USA) with a thickness of 25 µm was placed between the NMC 622 cathode and the Li-foil. A total amount of 120 µL of electrolyte, which consisted of ethylene carbonate (EC)/ethyl methyl carbonate (EMC) (3:7, vol%) with 1.3 M $LiPF_6$ as a conducting salt and 5 wt% fluoroethylene carbonate (FEC) as an additive, was added to each cell. Finally, the cell component stack was sealed using an electric crimper machine (MSK-160D, MTI Corporation, Richmond, CA, USA). The cells were stored at 20 °C after assembly for 24 h to ensure the complete wetting of the electrodes and separators.

Rate capability analyses as well as long-term cycle analyses were performed using a BT 2000 battery cycler (Arbin Instruments, College Station, TX, USA). The "constant current–constant voltage" (CCCV) method was applied during charging, while only a constant current was used during discharging. A specific capacity of 172 mAh/g with regard to the NMC 622 cathodes was applied for the calculation of the C-rate current. The term "C-rate" is defined as the ratio of the current at which a battery is charged or discharged to its nominal capacity. Thus, the current increases with an increasing C-rate, while the charge/discharge time decreases. For example, C/5 indicates the current applied to charge or discharge a cell in 5 h. During rate capability analyses, all cells were cycled three times at C/20, which was applied as the "formation" step. Afterward, the discharge C-rate was increased from C/10 to 3C. For discharge C-rates higher than C/2, the charge C-rates remained at C/2, while the same respective charge C-rate was applied at C/10 and C/5 discharge. At last, 5 cycles at C/5 were applied to study the capacity retention after fast charging/discharging. For the long-term cycle analyses, the cells were cycled 50 times with C/2 charging and 1C discharging directly after formation. In addition, cyclic

voltammetry (CV) was performed using a voltage window of 3.0–4.3 V versus Li/Li^+ and at different scanning rates increasing from 0.02 to 0.1 mV/s with a BCS-810 battery tester (BioLogic, Seyssinet-Pariset, France).

3. Results

The results of electrode preparation, laser patterning of the NMC 622 electrodes, and electrochemical characterization will be presented.

3.1. Electrode Preparation

The NMC 622 electrodes prepared with PVDF binder exhibit an active mass loading of 37.6 ± 0.8 mg/cm^2, which corresponds to an areal capacity of 6.5 ± 0.1 mAh/cm^2. This is more than twice as high as electrodes with a state-of-the-art mass loading [43]. The film thickness before and after calendering is 167 ± 5 µm and 154 ± 3 µm (without Al current collector), respectively. An SEM image of the surface of the NMC 622 cathode is shown in Figure 2a. The secondary NMC 622 particles (marked in red circles) surrounded by the conductive agent and binder are approximately 8.5 µm in diameter. A homogenous distribution of NMC 622 particles is observed in the cross-sectional view (Figure 2b). In addition, no significant interface due to the applied dual-layer coatings could be recognized, see Figure 2b,c. The cross-sectional view of the NMC 622 cathode with a fluorescent additive is shown in Figure 2c. The Al current collector and the NMC 622 particles are shown in red, while the green part is the resin that contains the fluorescent additive, which means that there is no electrode material. The calculated porosity of the thick-film NMC 622 electrodes is 36 ± 2%.

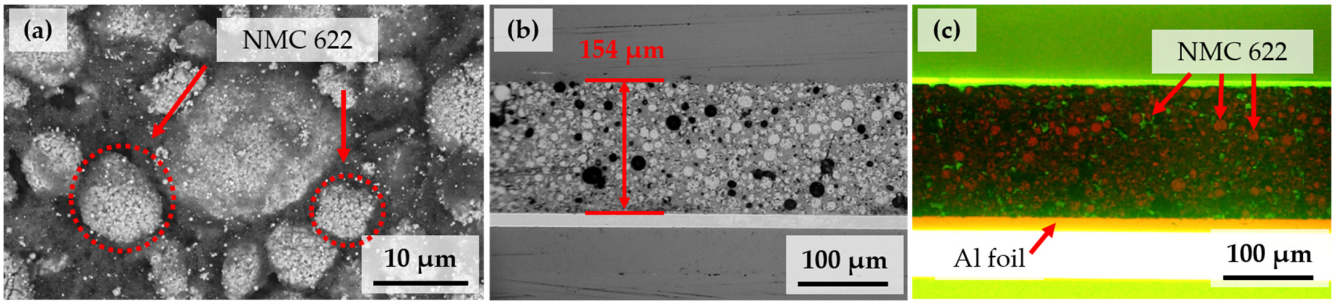

Figure 2. The NMC 622 electrode after drying using (**a**) SEM imaging from top of the electrode (red marked areas are typically secondary particles), and the cross-sectional views of a calendered electrode using (**b**) optical microscopy (black spots are due to sample preparation and are related to pores due to removed particles) and (**c**) a fluorescent additive.

3.2. Laser Patterning of NMC 622 Electrodes

In total, eight different pattern types were selected for laser patterning in this work. By adjusting the laser power, laser repetition rates, and number of scan passes, we aimed to keep the laser processing time as low as possible while achieving an adequate 3D electrode architecture with an acceptable mass loss lower than 10%.

Figure 3a,b display the laser-patterned NMC 622 electrodes with an L1 line pattern and a pitch of 200 µm. The maximum width at the electrode surface is 54 ± 1 µm, while the FWHM of the channels is 15 ± 2 µm. Without damaging the Al current collector, an aspect ratio of 11 is achieved for the L1 structure. The mass loss of laser-patterned electrodes is calculated from the weight difference between laser-patterned and unpatterned electrodes from the same electrode sheets, excluding the mass of the Al foil. The mass loss of laser-patterned L1 electrodes is 6.1 ± 2.8%.

Electrodes with an L2 pattern have the same pitch as those with L1 patterns, but the laser line energy used for L2 patterning is 3.2 times higher than that for L1, as shown in Table 1. Therefore, a higher maximum width of 66 ± 8 µm and an FWHM of 36 ± 4 µm are observed in Figure 3c,d, which leads to a mass loss of 11.3 ± 2.7%. Since the total ablation

depth remains the same, the aspect ratio decreases to 4.2. In addition, the ablation depth in calendered and uncalendered electrodes with an increasing number of laser scan passes was investigated, while the laser power was kept constant at 73 W and the laser repetition rate and the scanning speed were set to a constant 1.5 MHz and 10 m/s, respectively. Figure S1 depicts that with an increasing number of laser scan passes, the ablation depth shows a linear increase for both uncalendered and calendered NMC 622 electrodes. At around 26–28 scan passes, the current collector is exposed, indicating ablation depths of 6.2 µm and 5.7 µm per laser scan for uncalendered and calendered NMC 622 electrodes, respectively. However, considering the deviation in ablation depth, 25 scan passes were selected for the L2 patterning of calendered electrodes in order to avoid affecting the current collector.

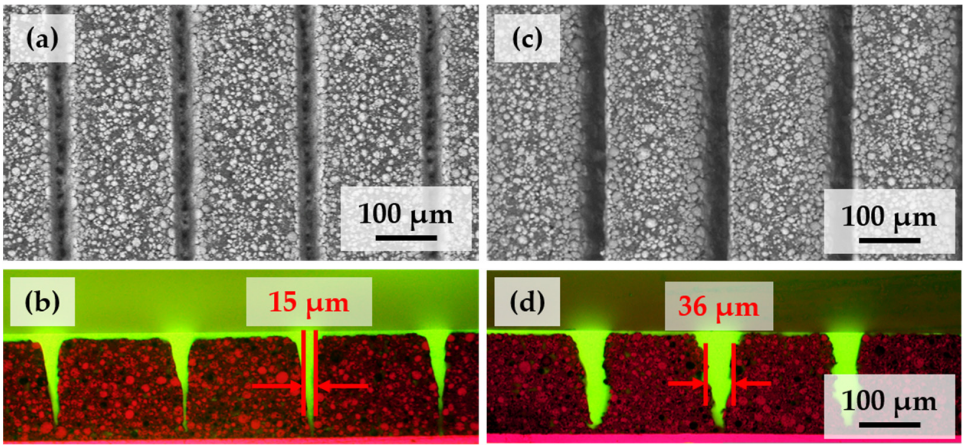

Figure 3. SEM images of laser-structured NMC 622 electrodes with (**a**) L1 and (**c**) L2 pattern types with narrow and broad channels, respectively, and (**b**,**d**) their cross-sectional views.

Furthermore, in order to investigate the effect of different laser energy inputs on the sidewall geometry of grooves, the samples were bent along a channel structure and the sidewalls were investigated via SEM, as shown in Figure 4a. With a low laser line energy and increasing scan passes, the groove surface in L1-patterned electrodes is quite smooth and polished, as depicted in Figure 4b, indicating a neglectable laser-induced thermal impact on the NMC 622 composite material. With an increasing laser line energy, the sidewalls show a distinctly heterogeneous surface structure. Figure 4c displays that secondary NMC 622 particles are observed along the upper the part of the electrode, while melting formation can be seen in deeper areas, which can be assigned to NMC 622 secondary particles covered with recondensed or melted PVDF binder. In addition, an interaction between the laser-generated plasma and the NMC 622 particles is possible, which can lead to a thermal impact and selective ablation during the laser process. However, to the best of our knowledge, detailed research on the sidewalls of battery materials after laser structuring has so far not been conducted and more studies in the future are necessary. However, a rough guideline can be extracted from the work of Dunlap et al. [23]. They found that no new phases were formed during the ablation process using an fs laser by comparing the XRD spectra with pristine NMC 622 powder, and they also measured the chemical composition of NMC 622 near the ablated channels using energy-dispersive X-ray spectroscopy (EDS) and found no signs of compositional changes. Although the selected analysis may not be surface-sensitive, it can be assumed that the thermal effect of laser processing on the NMC 622 particles for low and high line energies can be neglected in the first instance.

Figure 5 exhibits the laser-patterned electrodes with LiHo and GHo structures, which are the combination of broad lines and holes. In electrodes with an LiHo pattern, the pitch of lines is 450 µm, while the basic arrangement of holes can be described as equilateral triangles with a side length of 130 µm. In addition, NMC 622 secondary particles are clearly visible near the channels, as shown in Figure 5b, which is similar to the surface topography

of the sidewalls shown in Figure 4c. In addition, the current collector is exposed, indicating maximum material removal. The same laser parameter is applied for line patterning in electrodes with a GHo structure, while the length of the grids is adjusted to 750 µm with four holes spaced 250 µm apart in each grid. The mass loss of laser-patterned electrodes with LiHo and GHo structures is 6.7 ± 2.6% and 6.3 ± 2.6%, respectively.

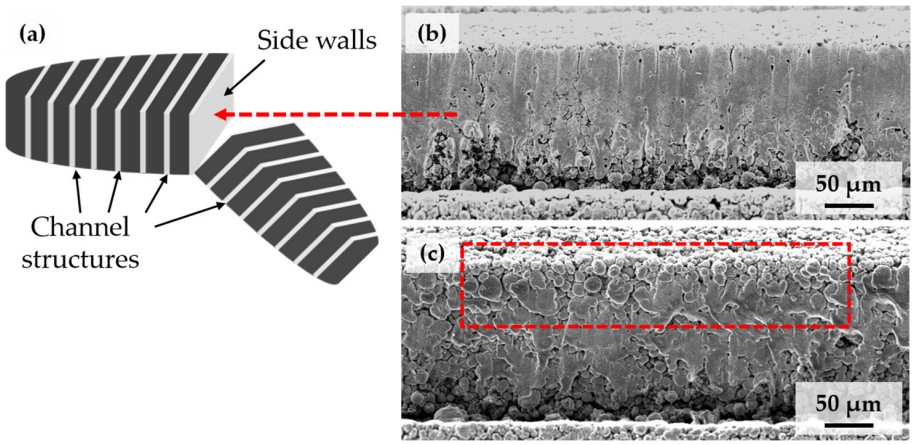

Figure 4. Investigation of the sidewall surfaces inside the channel structures. (**a**) A schematic view of the sample preparation, and the sidewalls in (**b**) L1- and (**c**) L2-patterned NMC 622 electrodes.

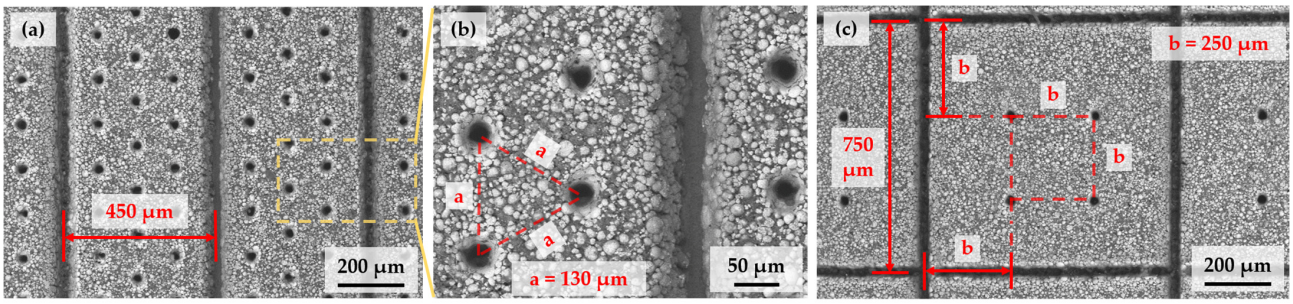

Figure 5. SEM images of laser-structured NMC 622 electrodes with (**a**,**b**) an LiHo structure and (**c**) a GHo structure.

For the laser patterning of hole structures, a different scanning strategy was applied in order to reduce the processing time. Since a pulsed laser with an adjustable laser repetition rate was applied, a constant distance of 100 µm between adjacent holes can be achieved by decreasing the laser repetition rate to 100 kHz while keeping a scanning speed of 10 m/s. As a result, 13,509 holes were generated in a cathode with a diameter of 12 mm. The hole diameter at the electrode surface is 43 ± 2 µm, while the FWHM of the hole structure is 15 ± 1 µm, as shown in Figure S2. A total number of scan passes of 70 was applied for the patterning of the holes, indicating an ablation depth of 2.2 µm per laser pulse, which is lower in comparison to that of L1 and L2 patterning. The mass loss of laser-patterned NMC 622 electrodes with an Ho structure is 7.4 ± 2.5%.

In order to generate hexagonal patterns inside the thick-film electrodes without affecting the current collector at the corners of hexagons, the laser power was decreased to 35 W, while the laser scanning speed was reduced from 10 to 5 m/s. To characterize the channel geometry, these laser parameters were first applied for patterning using a line pattern, as shown in Figure 6a. A maximum width of 57 ± 4 µm and an FWHM of 18 ± 1 µm were found for channel structures, and an aspect ratio of 8.4 was achieved, which is intermediate between that of L1 and L2 structures. Figure 6b,c exhibit the Hex structure and the alternative HexHo structure with a hole in each hexagon, respectively. No trace of current collector damage or modification was found at the corners of the hexagons

in SEM images. The calculated mass loss of the laser-patterned electrodes with Hex and HexHo structures is 6.5 ± 2.0% and 7.3 ± 2.4%, respectively. This implies an increase in mass loss of 0.8% due to addition of the hole structure.

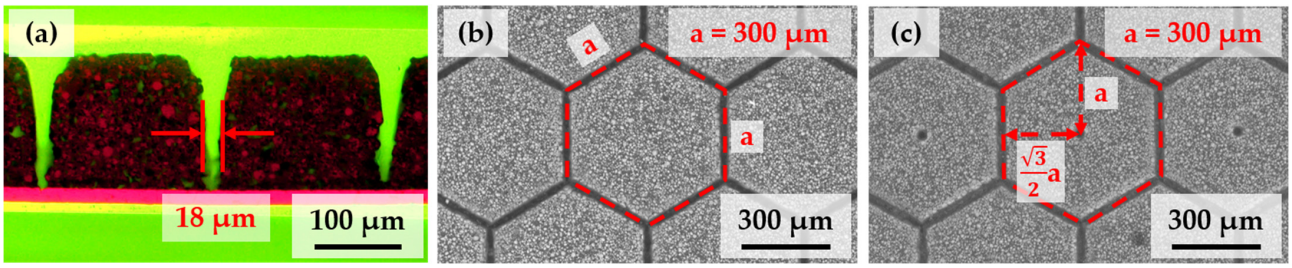

Figure 6. Cross-sectional view of (**a**) laser-patterned thick-film NMC 622 electrodes with a line structure using the same laser parameters for hexagonal patterning, and the SEM images of laser-patterned electrodes with (**b**) Hex and HexHo (**c**) structures.

Figure S3a shows the SEM image of an exposed side wall of a hexagonal structure. The surface of the sidewall resembles that of the L1 structure, with a smooth surface from the upper surface to a depth of about 90 µm. At the depth of around 110 µm, the sidewall surface is similar to those in L2-patterned electrodes. In addition, the surface of the hole shown in Figure S3b is similar to the side walls in L1-patterned electrodes with no melt formation or selective ablation. The boundaries of the NMC 622 secondary particles (marked in red) are clearly visible. The third variant of the hexagonal structures is shown in Figure S4a and b. The basic pattern is the same as the HexHo structure; thus, the same laser parameters were applied for laser patterning. The distance between adjacent hexagon centers corresponds to three time the inner distance from the central hole to the edge ($3\frac{\sqrt{3}}{2}a$, where a is the side length of a hexagon), as displayed in Figure S4b. The laser-patterned NMC 622 electrodes with a Sep.HexHo structure have a mass loss of 8.2 ± 2.1%, which is the highest in comparison to other hexagonal structures. This is because in the other two hexagonal patterns, neighboring hexagons share a common edge, while no shared edges exist in this design, thus leading to more material ablation.

3.3. Electrochemical Characterization

The laser-patterned NMC 622 cathodes were assembled in coin cells and electrochemically characterized using rate capability analyses, long-term cycle analyses, and cyclic voltammetry.

3.3.1. Rate Capability Analyses

The specific discharge capacities of cells containing unpatterned NMC 622 cathodes (reference electrodes) and laser-patterned electrodes with L1, L2, and LiHo structures at different C-rates varying from C/20 to 3C are plotted in Figure 7. In the first formation cycle, cells containing laser-patterned electrodes with L1 and LiHo structures and reference electrodes exhibit a similar specific discharge capacity of 171 mAh/g, while those with L2-patterned electrodes show a lower initial capacity of 169 mAh/g. In addition, the initial coulombic efficiency (ICE) from the first cycle was determined by dividing the discharge capacity by the charge capacity. Reference cells exhibit the lowest ICE of 87.7 ± 0.4%, while the ones with L1 and L2 line patterns show an ICE of 88.5 ± 0.2% and 88.3 ± 0.3%, respectively. After adding holes to the line structure, the ICE increases to 88.8 ± 0.1% for cells containing electrodes with an LiHo structure. When the C-rate increases to C/10, all cells show a similar capacity of 165 mAh/g, while at C/5, the reference cells exhibit about a 2 mAh/g lower discharge capacity in comparison to other cells. At C/2, all cells with laser-patterned electrodes begin to show enhanced electrochemical properties, displaying a capacity of around 150 mAh/g, while the reference ones reach a 130 mAh/g capacity. The capacity difference between reference cells and those with laser-patterned electrodes

becomes more obvious at 1C, where the cells with L2-patterned electrodes show the highest capacity, followed by those with LiHo and L1 structures. The reference cells exhibit a capacity of around 50 mAh/g, which is almost 70 mAh/g lower than the capacity of other cells with laser-patterned electrodes. At 2C, the cells with 3D electrodes have a 10–18 mAh/g higher capacity in comparison to the reference ones, while at 3C, a capacity increase of 8 mAh/g is observed for all cells with laser-patterned electrodes. After being cycled again at C/5, cells with an LiHo structure show the highest capacity retention, while the reference cells exhibit the lowest capacity retention.

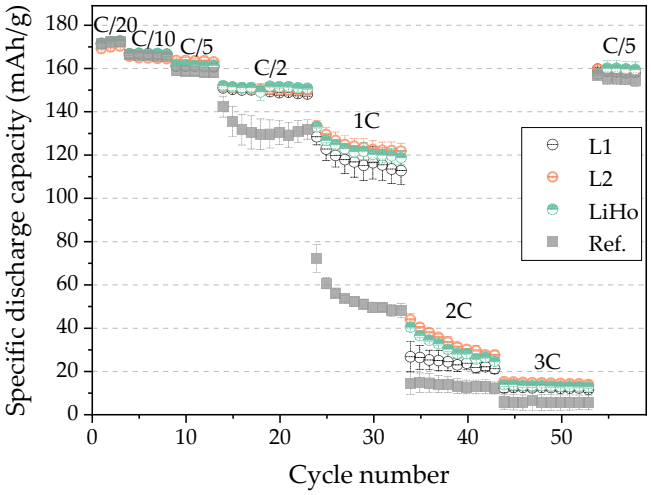

Figure 7. Rate capability analyses of cells containing reference NMC 622 electrodes and laser-structured electrodes with L1, L2, and LiHo structures at C-rates ranging from C/20 to 3C.

The rate capability of cells containing laser-structured electrodes with other structures is shown in Figure 8. Cells with GHo- and Ho-patterned NMC 622 electrodes achieve a similar capacity of 172 mAh/g at C/20, as displayed in Figure 8a. The ICE of cells with GHo- and Ho-patterned electrodes is 88.4 ± 0.5% and 89.2 ± 0.2%, respectively. The cells with an Ho structure achieve the highest ICE compared to other cells.

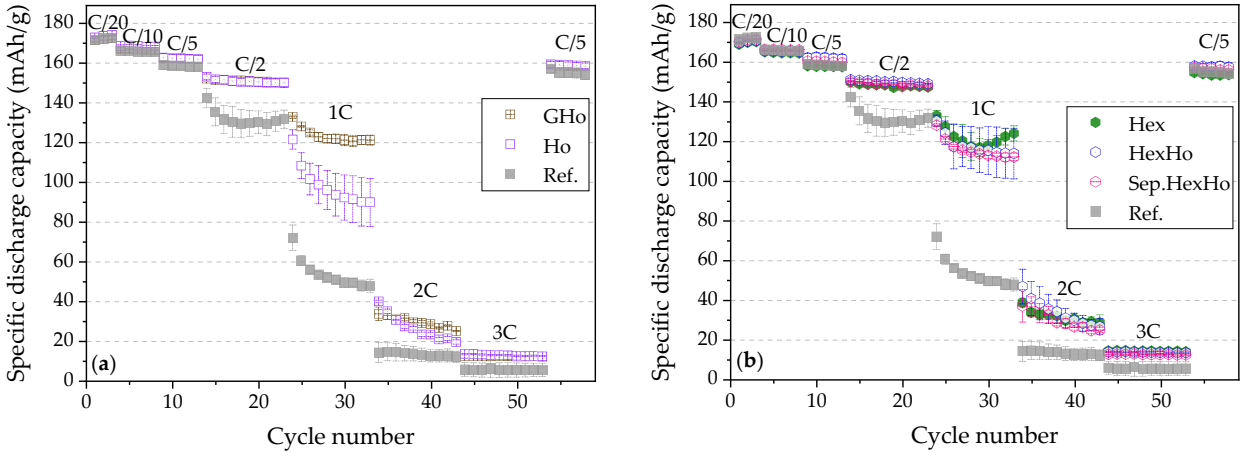

Figure 8. Specific discharge capacity of cells containing laser-structured NMC 622 electrodes with (**a**) GHo and Ho structures, and with (**b**) Hex, HexHo, and Sep.HexHo structures at C-rates varying from C/20 to 3C in comparison to reference cells.

At C/10 to C/2, a similar discharge capacity is achieved by cells with GHo- and Ho-patterned electrodes in comparison to those with line structures. However, at 1C, cells with Ho-patterned electrodes exhibit a more severe degradation, with the discharge capacity

dropping from 121 to 90 mAh/g, while cells with GHo-patterned electrodes maintain a capacity of 121 mAh/g after 10 cycles, which is a similar value to the cells containing laser-patterned electrodes with an L2 structure. In addition, cells with Ho-patterned electrodes show high-capacity deviation at 1C, indicating an unstable electrochemical performance of electrodes with an Ho structure. At 2C, cells with GHo-patterned electrodes show about a 4 mAh/g higher capacity in contrast to those with an Ho structure, while at 3C, both cells with laser-patterned electrodes have a 12 mAh/g capacity, which is 7 mAh/g higher than that of the reference cells. After being cycled again at C/5, cells with both GHo- and Ho-patterned electrodes reach a similar capacity of 159 mAh/g.

The cells containing laser-patterned electrodes with different hexagonal structures are presented in Figure 8b. The initial capacity of all cells with electrodes of different hexagonal structures is 170 mAh/g. The cells with Hex-patterned electrodes show an ICE of 88.0 ± 0.3%, while the ones with HexHo- and Sep.HexHo-patterned electrodes exhibit an ICE of 88.7 ± 0.1% and 88.1 ± 0.3%, respectively. At C/10, cells with Sep.HexHo-patterned electrodes show the highest capacity of 166 mAh/g, while the ones with HexHo and Hex patterns exhibit a lower discharge capacity. At a higher C-rate of C/5, cells with HexHo-patterned electrodes maintain the highest capacity of 162 mAh/g, while those with a Hex structure show a discharge capacity of 158 mAh/g. At C/2, no obvious difference in the discharge capacity is observed between different hexagonal structures. However, at 1C, cells with Hex-patterned electrodes show a capacity decrease from the first cycle to the sixth cycle (133 to 117 mAh/g) and then a slight increase to 124 mAh/g until the last cycle at 1C, while other cells experience a continuous capacity decrease from 130 to 113 mAh/g. The capacity increase at high C-rates has been observed in previous works [22,42]. The reason for this behavior is still unclear and deserves more research in the future. At 2C, cells with HexHo-patterned electrodes exhibit the highest discharge capacity, while at 3C, all cells have a capacity of around 12 mAh/g, losing more than 90% capacity in comparison to the initial capacity at C/20. After being cycled again at C/5, cells with a HexHo structure retain the highest capacity, while those with Hex structures exhibit a lower capacity than the reference cells.

3.3.2. Long-Term Cycle Analyses

In addition to the rate capability test, some cells containing laser-patterned electrodes were cycled at C/2 charge and 1C discharge after the formation step to analyze their lifetime at high C-rates.

After formation, the cell with unpatterned cathodes shows the highest specific discharge capacity of 175 mAh/g, while those with laser-patterned electrodes exhibit capacities between 168 and 172 mAh/g, as shown in Figure 9. When discharged at 1C, the specific capacity of the reference cell suddenly drops to 122 mAh/g and is further reduced to 102 and 94 mAh/g in the second and third cycle, respectively. From the third cycle to the last cycle, the reference cell shows a stable behavior, and a specific capacity of 80 mAh/g is reached at the end of long-term cycle analysis after 50 cycles. As for cells with laser-patterned electrodes, the one with an LiHo-patterned electrode displays the highest capacity of 146 mAh/g at the first 1C cycle, while the ones with a HexHo and Ho structures display the lowest capacity of 136 mAh/g. Cells with other L2- and L1-patterned electrodes show discharge capacities of 144 and 141 mAh/g at the first 1C cycle, respectively. In addition, it was noted that after laser patterning, the sudden capacity drop at the beginning of 1C cycling disappeared. The cell with L1-patterned cathodes suffers the most severe capacity loss of 52 mAh/g after cycling in comparison to its initial capacity at 1C, losing about 37% of its capacity.

The initial and final discharge capacities of cells containing laser-structured electrodes with different pattern types and the reference cell are summarized in Table 2. All cells with laser-patterned electrodes exhibit higher initial and final capacities than those of the reference cell. In addition, the cells containing LiHo- and Ho-patterned electrodes show the highest capacity retention of 83% compared to their initial capacity, followed by those

with an L2 structure. Cells with a HexHo structure show a 76% capacity retention, which is 10% higher than that of the reference cells. However, although the cell with an L1 pattern exhibits 19 and 9 mAh/g higher initial and final discharge capacities compared to the reference cell, respectively, it retains the lowest capacity in comparison to all other cells after 50 cycles.

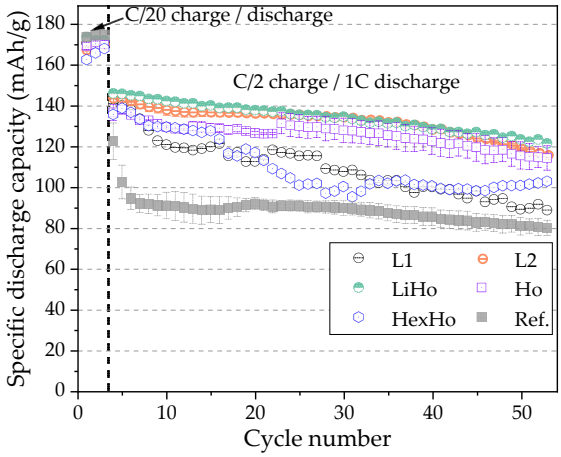

Figure 9. Long-term cycle analysis of cells containing laser-structured NMC 622 electrodes with different structures in comparison to the reference cell using C/2 charging and 1C discharging after formation at C/20.

Table 2. Initial and final discharge capacities of cells containing unstructured electrodes (Ref.) and laser-structured electrodes with different pattern types and their capacity retention during long-term cycle analyses.

Pattern Types	Initial Discharge Capacity (mAh/g)	Final Discharge Capacity (mAh/g)	Capacity Retention (%)
L1	141	89	63
L2	144	116	81
LiHo	146	121	83
Ho	137	114	83
HexHo	136	103	76
Ref.	122	80	66

3.3.3. Cyclic Voltammetry

The effective Li-ion diffusion coefficient of cells containing laser-patterned NMC 622 and NMC 811 electrodes with line structures has been studied using a CV analysis [22,26], while hole structures were reported for graphite anodes [24,33,34,36], NMC 622 cathodes [24], and LFP cathodes [31,33]. However, hexagonal structures have never been investigated. Thus, in this work, CV analyses were performed on the reference cell and the cell containing HexHo-patterned NMC 622 electrodes using scan rates ranging from 0.02 to 0.10 mV/s, as displayed in Figure 10.

At a scan rate of 0.02 mV/s, the reference cell reaches a maximum current of 1.73 mA at 3.83 V during charging and −1.31 mA at 3.63 V during discharging, while the cell with a HexHo-patterned electrode exhibits a higher maximum current of 2.05 mA at lower voltage (3.78 V) during charging and a lower discharge peak current at 3.67 V. With an increasing scan rate, the maximum current of all cells increases and shifts to a higher voltage during charging, while that during discharging moves in the opposite direction. The peak-to-peak separation (voltage difference) for the reference cell increases from 0.20 to 0.52 V with an increasing scan rate, while that of the cell containing a laser-patterned electrode with a HexHo structure increases from 0.11 to 0.34 V, indicating that the peak separation is reduced after laser patterning.

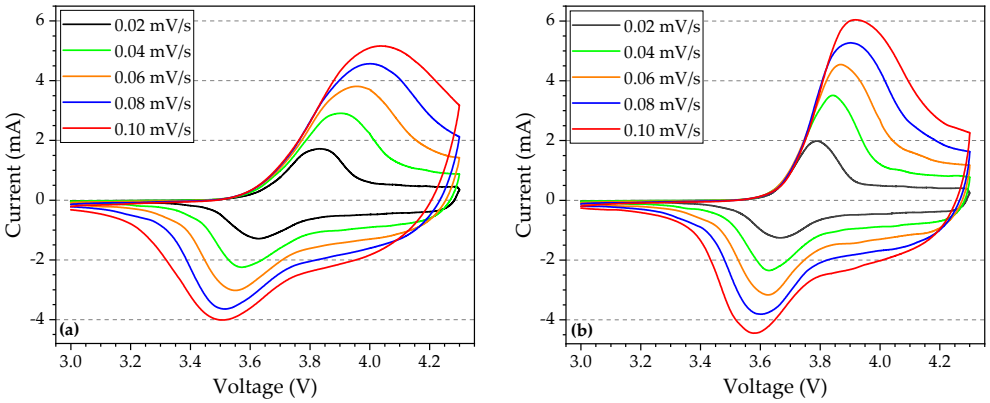

Figure 10. CV plots of cells with (**a**) an unstructured electrode and (**b**) a laser-patterned electrode with a HexHo structure using scan rates ranging from 0.02 to 0.10 mV/s with a voltage window of 3.0–4.3 V.

4. Discussion

The results of the electrochemical analyses of cells containing laser-structured thick-film NMC 622 electrodes with different structure types will be discussed. Meanwhile, the effective Li-ion diffusion coefficient will be calculated from the results of the CV analysis to determine the Li-ion diffusion kinetics. Furthermore, the efficiency of laser patterning using different patterns will be analyzed.

4.1. The Effect of Laser Patterning on the Electrochemical Performance

A narrow line structure with a pitch of 200 µm has been investigated in our previous research (see [22] and the references cited therein) and was applied as the baseline for laser patterning (L1 pattern). In order to further enhance the electrochemical performance, different structures were applied in the laser patterning of NMC 622 electrodes. In addition, expcept for L2 and Sep.HexHo structures, the mass loss caused by laser patterning with other structures was adjusted to approximately 7%, which is lower in comparison to other published works by 11–20% [21,23]. The purpose of using the L2 pattern is to explore the effect of the channel width on the electrochemical performance and to explore the possibility of reducing the laser processing time. The total electrode surface area and the increase in electrode surface area due to laser structuring using different pattern types in comparison to the unstructured electrodes are listed in Table S1. The total electrode surface area was estimated using the maximum width and the FWHM from cross-sectional analyses shown in Figures 3b,d and 6a. Laser-structured electrodes with an L1 pattern exhibit the highest surface area increase of 130%, followed by L2- and Ho-structured electrodes, while those with a GHo pattern display the lowest surface area increase of 71%.

Rate capability analyses show that at low discharge C-rates from C/20 to C/5, no clear capacity increase is observed for cells with laser-patterned electrodes, which is similar to other published results [22,24,26]. The reason for this is that at C-rates $\leq$ C/5, the discharge capacity is mainly affected by ohmic losses and the charge transfer resistance, while at C-rates > C/5, lithium-ion transport in the electrolyte inside the composite electrode limits the cell performance due to cell polarization [44]. Figure 11 presents the increase in the specific discharge capacity of cells with laser-patterned electrodes in contrast to the reference cells at four C-rates ranging from C/10 to 2C. At C/10, cells with laser-patterned electrodes exhibit a less than 1% capacity difference compared to the reference cells, while at C/2, a capacity increase of about 16–19 mAh/g is observed for cells with laser-patterned electrodes. A maximum capacity increase of 14% is observed for cells with LiHo, GHo, and Ho structures at C/2, followed by those with an L2 structure. Cells with a Hex structure show a 12% capacity increase. However, after combining the Hex and hole structures, the capacity can be further increased to 14%, while only a 0.8% higher mass loss is caused by introducing the hole structure into the existing hexagonal structure.

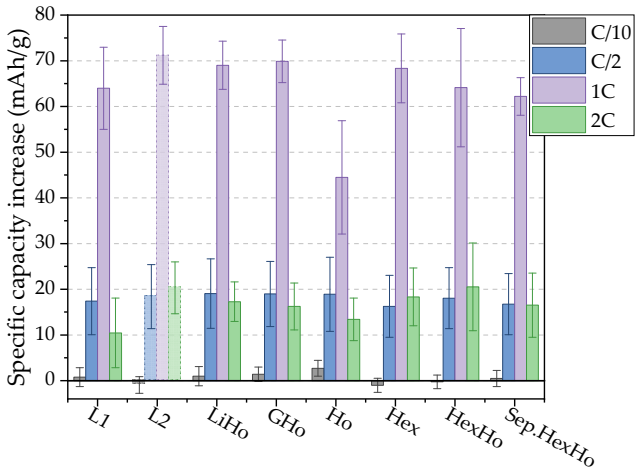

Figure 11. Specific discharge capacity increase for cells containing laser-patterned electrodes with different structure types at C/10, C/2, 1C, and 2C in contrast to reference cells.

For cells containing thick-film NMC 622 electrodes with a thickness of 154 µm, the maximum capacity increase after laser patterning is observed at 1C. For example, cells with an L2 structure show the highest capacity increase of 71 mAh/g, while those with GHo and LiHo structures achieve the second and the third highest capacity increase, respectively. In comparison to electrodes with an L1 structure, those with an L2 structure have a 5% higher mass loss after laser structuring and a higher rate capability at C/2, 1C, and 2C. This is in good agreement with the study of Heubner et al. [5], which shows that the power density increases with an increasing electrode porosity, since a higher mass loss can be equated with a higher porosity inside the electrode. Furthermore, the mass loss after applying the L2 structure is much higher than that of other structures and should be excluded. Thus, the optimal structures to maximize capacity at 1C are the LiHo and GHo structures. In addition, cells consisting of only a hole structure exhibit a minimal capacity increase of 44 mAh/g at 1C in contrast to other cells, but by combining holes with lines, grids, or hexagonal structures, a further capacity increase of 37–47% can be achieved. Another interesting fact is that when comparing different hexagonal structures, it was found that the discharge capacity increase at 1C reduces with an increasing mass loss, which is contrary to previously reported results [22]. For example, cells containing Sep.HexHo-patterned electrodes show the minimal capacity increase of 62 mAh/g in comparison to those with other hexagonal structures, but have the highest mass loss due to laser patterning. At 2C, cells with HexHo-patterned electrodes exhibit the highest capacity increase of 21 mAh/g in comparison to cells with other patterns, while those with an L1 structure reach the lowest capacity increase of 10 mAh/g. Aside from L2, applying HexHo structures can maximize the capacity increase at 2C. Therefore, in addition to the mass loss, the geometrical design of the structures affects the electrochemical performance of cells with laser-patterned electrodes, especially at C-rates above C/2. Thus, it is necessary to select an appropriate structure for laser patterning according to the requirements of the discharge C-rates in practical applications.

The approach of combining lines, grids, and hexagonal structures with holes is based on our previous results [45], where a reduced Li concentration was observed in the center of free-standing square-shaped micro-pillars of NMC 111 (0.6 mm × 0.6 mm × 0.1 mm, length × width × height) after 2C charging and discharging. In addition, the Li concentration decreases rapidly with an increasing distance from the upper surface to the bulk electrode, which means that more active materials are inactive and no longer have an influence on the electrochemical performance at high C-rates. However, by combining holes with lines or hexagonal structures, the holes can serve as an electrolyte reservoir and activate more NMC 622 particles during charging and discharging, while channel structures can accelerate the wetting of the electrolyte in the bulk electrode [18,19], leading

to a more homogenous electrolyte distribution in the electrode. In addition, when we compare the capacity increase of cells containing laser-patterned electrodes with different structure types and their surface area increase, as listed in Table S1, no clear relationship can be found. For example, laser-structured electrodes with L2 and Ho patterns show a similar surface area increase of about 123%, but their electrochemical performances are very different, especially at C-rates higher than C/5 (Figure 11). It is therefore assumed that the increase in electrode surface area due to laser structuring is not directly related to the capacity enhancement.

In order to further investigate the advantage of combining lines or hexagons with holes, the charge and discharge curves of cells containing laser-structured cathodes with different structure types from the second cycle at C/10 and 1C are displayed in Figure 12. All cells reach similar capacities of 165–168 mAh/g after being discharged at C/10 to 3.0 V. In addition, all cells with laser-patterned electrodes show a lower cell polarization in comparison to the reference cell by discharging before 160 mAh/g, since their discharge plateaus are higher than that of the reference, as displayed in Figure 12a,b. In addition, a fast voltage drop (IR-drop) at the beginning of each discharge curve is observed. All cells with laser-patterned electrodes have an IR-drop of 0.04 V at C/10, which is lower than that of the reference, at 0.07 V, indicating a lower cell polarization.

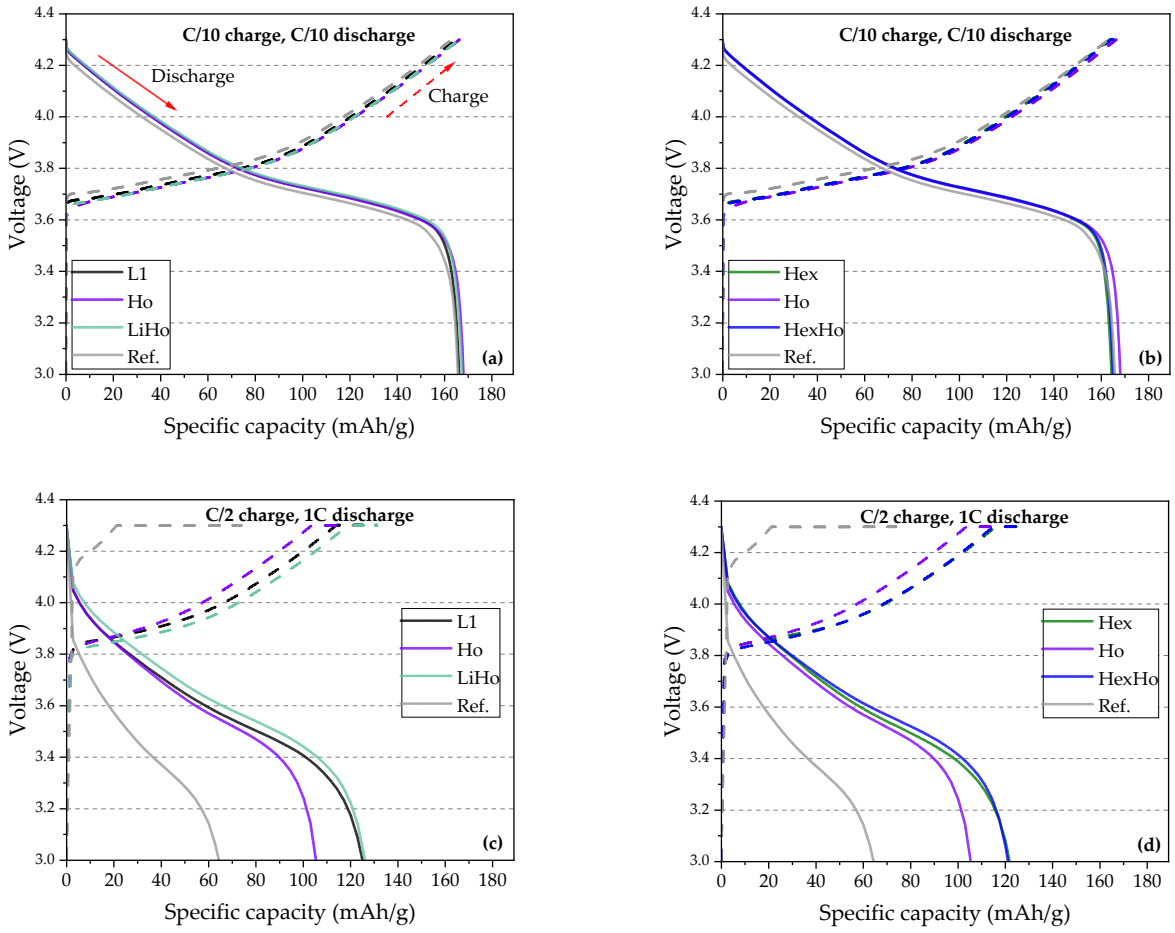

Figure 12. Comparison of the specific capacity versus voltage of cells containing laser-patterned NMC 622 electrodes with different structure types as well as the reference cell at (**a**,**b**) C/10 charging and discharging, and at (**c**,**d**) C/2 charging and 1C discharging.

During C/2 charging, as shown in Figure 12c,d, the capacity originating from the constant-voltage phase (horizontal plateau at the end of charge) is more than 70% of the total capacity of the reference cell, while this share is reduced to about 10% for cells with

laser-patterned electrodes. This indicates that without laser patterning, the charging time of the cells is considerably extended, while at the same time, only half the capacity is achieved. As for 1C discharging, an IR-drop of 0.45 V is observed for the reference cell, while the cell with an LiHo-patterned electrode shows the lowest IR-drop of 0.22 V. Cells with L1- or Ho-patterned electrodes have the same voltage drop of 0.25 V, while those with Hex and HexHo structures exhibit a similar IR-drop of 0.23 V. The combination of line and holes has a synergistic effect and can lead to a lower ohmic resistance than that achieved when applying only one kind of structure. For example, the cell with an L1-patterned electrode has a higher discharge plateau between 20 and 125 mAh/g than the one with an Ho structure (Figure 12c), which indicates a reduced cell polarization for cells with an L1 structure. In addition, the polarization further decreases for cells with an LiHo structure at 3 to 125 mAh/g. A similar phenomenon is observed in Figure 12d after combining a hole structure with a hexagonal structure. The geometrical changes in laser-patterned thick-film electrodes contribute to reduced electronic and ionic resistances and a decreased tortuosity [25]. In addition, the Li-ion diffusion kinetics are increased due to the channels and holes generated inside laser-patterned electrodes filled with a liquid electrolyte [46,47].

The long-term cycle analysis in Figure 9 shows that the cell with electrodes with an LiHo pattern maintains the highest ICE and the highest capacity, which proves that by combining lines and holes, the cell's lifetime can be further extended while keeping the mass loss constant. As for the reference cell, the fast capacity drop in the first five cycles at 1C must be due to the high internal resistance and the poor mechanical integrity of the thick-film electrodes [48] and the serious reaction inhomogeneity [6]. However, a fast capacity fade in the rate capability analysis of cells containing an Ho structure at 1C is not observed in the long-term cycle analysis. This might be explained by the fast ageing of cells with an Ho structure after being cycled at different C-rates. However, it has been reported that there are significant differences in the electrochemical stability between half cells assembled with cathodes from the same electrode sheet [49]. Therefore, further experiments on full cells containing laser-patterned NMC 622 cathodes versus graphite anodes will be conducted in our future work to provide more convincing results with regard to the lifetime assessment.

CV analyses of the reference cell and the cell with an HexHo-patterned electrode in Figure 10 display only one anodic and cathodic peak for all cells at each scan rate, which corresponds to the redox reaction of $Ni^{2+}/Ni^{3+}/Ni^{4+}$ [50] and the phase transition of NMC 622 from a monoclinic to a hexagonal phase during discharging and vice versa [51]. In addition, the effective diffusion coefficients of Li-ions in cells can be determined from the CV analyses using the Randles–Ševčík equation, which has been illustrated in other works [22,52]. The specific maximum currents obtained from the CV analyses are plotted versus the square root of scan rates and a linear relation is found, as shown in Figure S5. The D_{eff} values summarized in Table 3 are consistent in magnitude with our previous results [22], but with slightly lower values, which must be due to the higher mass loading used in this work. D_{eff} during charging is higher than during discharging for all cells, indicating a faster Li-deintercalation in NMC 622 particles than intercalation. Furthermore, the D_{eff} of cells with a HexHo-patterned electrode is 45% and 17% higher than that of the reference cell during charging and discharging, respectively. On the one hand, this suggests an enhanced fast charging ability of cells containing laser-structured electrodes with a HexHo pattern in contrast to cells with unstructured electrodes. On the other hand, higher effective diffusion coefficients lead to an increased capacity, especially at C/2 to 2C, as exhibited in Figure 11.

Table 3. The effective Li-ion diffusion coefficients of cells with a reference electrode and a HexHo laser-patterned electrode during charging and discharging.

	Ref.	**HexHo**
D_{eff}—charge (cm^2/s)	1.22×10^{-13}	1.77×10^{-13}
D_{eff}—discharge (cm^2/s)	8.41×10^{-14}	9.84×10^{-14}

4.2. Evaluation of the Laser Patterning Process with Different Patterns

Previously, we discussed the effect of different patterns on the electrochemical performance. However, in industrial production, the efficiency of laser patterning is also important and cannot be neglected.

Table 4 summarizes the processing time required for laser structuring of the thick-film electrodes with eight different patterns. The processing time is divided into two parts: calculating the processing time for basic patterns ($t_{patterns}$), such as lines, grids, or hexagons, and the hole patterning time (t_{holes}). It should be noted that $t_{patterns}$ depends only on the geometry of the patterns, while the sequence and direction of the laser scanning paths are not taken into account. The processing time t is calculated from the total number of laser scan passes N (shown in Table 1), the total length of lines for each pattern L per 1 cm^2, and the applied laser scanning speed $v_{Scanning}$:

$$t = \frac{N \cdot L}{v_{Scanning}} \quad (1)$$

The area processing rate v_{area} is determined by dividing the unit area (1 cm^2) by the total processing time and can be used to compare the efficiency of laser patterning using different structure types. The mass loss resulting from laser patterning using different structure types is also listed in the following table.

Table 4. Comparison of the mass loss and processing time per unit area (1 cm^2) for the laser structuring of thick-film NMC 622 cathodes with different structure types and their area processing rates.

Structure Type	Mass Loss (%)	$t_{patterns}$ (s)	t_{holes} (s)	v_{area} (cm^2/s)
L1	6.1 ± 2.8	1.53	-	0.65
L2	11.3 ± 2.7	1.25	-	0.80
LiHo	6.7 ± 2.6	0.56	4.46	0.20
GHo	6.3 ± 2.6	0.67	1.73	0.42
Ho	7.4 ± 2.5	-	8.08	0.12
Hex	6.5 ± 2.0	1.95	-	0.51
HexHo	7.3 ± 2.4	1.95	2.69	0.22
Sep.HexHo	8.2 ± 2.1	1.39	1.80	0.31

L1 and L2 structures have the same pitch, which means that the total scanning length is the same for these two structures. However, by increasing the laser power and reducing the number of scan passes, the processing time for L2 is 18% lower than that for L1. L2 patterning achieves the highest area processing rate in comparison to laser patterning with other structures, while patterning with a hole structure exhibits the lowest efficiency of 0.12 cm^2/s. However, L2 patterning leads to a 5.2% higher mass loss in comparison to that of L1, which is much higher than other patterns. Despite the trade-off between the laser processing efficiency and the loss of active materials using line structures, the parameters of laser patterning can be further optimized according to the acceptance of mass loss in practical applications and the required charge and discharge capacity of batteries at different C-rates.

The low area processing rate, as well as low discharge capacity increase (Figure 11), in comparison to other patterns does not favor the laser patterning of thick-film NMC 622 cathodes using the Ho structure. However, the patterning efficiency could be improved by increasing the pitch between the holes or increasing the laser power. Yamada et al. [33] reported on the roll-to-roll laser patterning of graphite anode with through-holes using a hollow cylinder. In their study, thin-film anodes with a thickness of 35 µm were laser patterned using a single scan, and a delivery rate of 2.6 m/min was achieved. However, the electrode thickness in this work is 5 times higher in comparison to their work. If a single scan was adopted for the hole patterning of thick-film electrodes, it would be necessary to greatly reduce the scanning speed while increasing the laser power, which would result

in an extremely high mass loss (estimated to be more than 20%). Thus, this method is not suitable in this work. Furthermore, the processing time for holes is much longer than for basic patterns. For example, despite a wide pitch of 450 µm, LiHo laser patterning achieves an area processing rate of 0.20 cm^2/s, which is only 1/4 as high as L2 patterning. Therefore, considering the laser patterning efficiency, patterns consisting of lines are more suitable for industrial applications and upscaling.

Since laser patterning was carried out using one scanner in this work, the hexagonal structures could only be realized at a reduced laser scanning speed due to their complex geometry. The adopted scanning strategy is displayed in Figure 13a; the upper edges of hexagons were laser patterned, followed by the lower edges, and, finally, parallel lines with a length of 280 µm were generated to avoid affecting the current collector at the corners of the hexagons. Although the laser scanning speed had to be reduced from 10 to 5 m/s, Hex patterning has the third highest area processing rate of 0.51 cm^2/s, which is only slower than that achieved using the other two line patterns. In order to further optimize the laser patterning efficiency, a polygon scanner system with three scanners could be applied, as shown in Figure 13b. Each scanner only needs to complete line patterns, while the edges of the hexagons can be realized by turning the laser on and off. In addition, interference between different laser beams can be avoided by using differently polarized laser beams for each scanner.

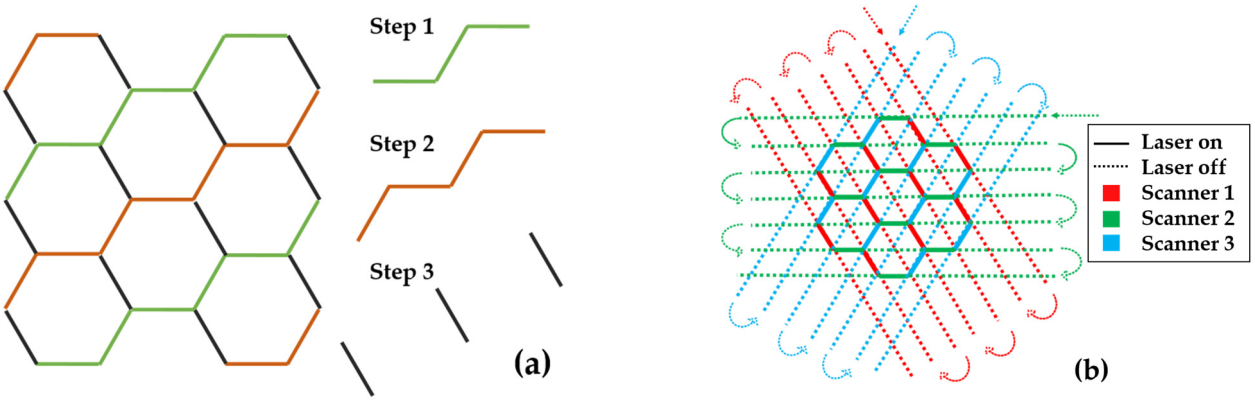

Figure 13. Schematics of (**a**) the applied scanning strategy and (**b**) a possible time-efficient scanning strategy with multiple scanners for the laser patterning of hexagonal structures.

5. Conclusions

Thick-film NMC 622 cathodes with a PVDF binder were prepared using a roll-to-roll coater with a dual-layer coating technique. A film thickness of 154 µm after calendering was achieved, which corresponds to an areal capacity of 6.5 mAh/cm^2. Afterward, laser patterning was performed on electrodes with eight different structure types using ultrafast laser ablation. Lines, grids, and hexagons were selected as the basic patterns, while the combinations of these patterns with holes were also realized. The ablation depths of the different structures of laser-patterned electrodes in this work were limited to the film thickness to avoid affecting the current collector.

In order to obtain comparable electrochemical results from cells containing electrodes patterned with different structures, the mass loss of all laser-structured electrodes was kept similar, at around 7%, by adjusting the designs of the different patterns, except for the L2 structure. With an increasing laser power, the channel width in L2-patterned electrodes becomes larger and the mass loss increases by 5% in comparison to L1-patterned electrodes with a low laser power and more laser scan passes. An SEM analysis reveals that the sidewalls of the channels in L1-patterned electrodes are smoother than those in L2-patterned electrodes, while secondary NMC 622 particles are observed near the upper surface of L2-patterned electrodes. Additionally, zones of either binder melting, material recondensation, or heat impact are found halfway through the film. The same laser

parameters as the L2 structure were further applied for the patterning of lines with LiHo and GHo structures, while holes were generated by adjusting the laser scanning speed as well as the laser repetition rate. In addition, hexagonal structures combined with holes and with a varied distance between adjacent hexagons were laser patterned in this work.

Rate capability analyses reveal that cells with laser-structured electrodes begin to show an enhanced performance at C-rates above C/2 compared to the reference cells. For example, all cells with laser-patterned electrodes exhibit a 16–19 mAh/g capacity increase at C/2; however, the effect of different patterns on the discharge capacity is not obvious. When the C-rate increases to 1C, the maximum capacity increase is observed, where cells with L2-, GHo-, LiHo-, and Hex-patterned electrodes achieve a capacity of about 70 mAh/g, an increase of 130% in comparison to reference cells. In contrast, cells containing hole-patterned electrodes show the lowest increase in the discharge capacity (45 mAh/g) and a higher cell polarization than cells with other pattern types. At 2C, Hex and HexHo structures exhibit the maximum discharge capacity, with an increase of 18–20 mAh/g, which indicates that hexagonal structures are a suitable choice for increased discharge capacities at high C-rates. This is further evidenced by CV measurements, where the cell with a HexHo-patterned electrode shows higher effective Li-ion diffusion coefficients in both the charging and discharging processes than the reference cell. Long-term cycle analyses conclude that the cell with an LiHo structure maintains a higher capacity than those with only holes or lines after cycling. This synergistic effect of combining holes with other patterns provides a new strategy for the laser patterning of electrodes.

In addition, the laser processing efficiency of different patterns is also discussed. The advantage of applying a high laser power and a lower number of laser scan passes (L2 patterning) is that it achieves the highest area processing rate, while laser patterning with an Ho structure has the lowest efficiency. In addition, the processing time for holes is much longer than for basic patterns, e.g., in LiHo and GHo patterning. Therefore, the laser patterning of ultra-thick-film cathodes with only holes is not desirable in terms of the processing efficiency and the electrochemical performance, while line patterns are more suitable for industrial applications and upscaling. In addition, an innovative laser scanning strategy is introduced to accelerate the laser patterning of hexagonal structures.

Supplementary Materials: The following supporting information can be downloaded at: https://www.mdpi.com/article/10.3390/batteries10020058/s1, Figure S1: Laser ablation depth in calendered and uncalendered NMC 622 electrodes with an increasing number of laser scan passes using laser parameters for L2 patterning. Figure S2: SEM images of laser-structured electrodes with an Ho structure providing a periodicity of a = 100 µm (equilateral triangle). Figure S3: SEM images of (a) a sidewall of laser-patterned NMC 622 electrodes with an HexHo structure and (b) the cross-sectional view of a hole in the center of a hexagonal pillar. Figure S4: SEM images of laser-structured NMC 622 electrodes with a Sep.HexHo structure. (a) A hexagon with a central hole and (b) the distance between adjacent hexagons. Figure S5: The maximum specific current versus the square root of scan rates for the reference cell and those with laser-structured NMC 622 cathodes with a HexHo pattern type. Table S1: The total surface areas of laser-structured electrodes with different pattern types and the surface area increase in comparison to the unstructured electrode.

Author Contributions: Conceptualization, P.S., P.Z. and W.P.; methodology, P.S. and P.Z.; validation, B.E., P.S., P.Z. and W.P.; formal analysis, B.E.; investigation, B.E. and P.S.; resources, B.E.; data curation, B.E. and P.Z.; writing—original draft preparation, P.Z. and WP.; writing—review and editing, B.E., P.S. and W.P.; visualization, B.E. and P.Z.; supervision, P.S., P.Z. and W.P.; project administration, W.P.; funding acquisition, W.P. All authors have read and agreed to the published version of the manuscript.

Funding: This research was funded by the German Research Foundation (DFG), project Hi-LiB (Process scaling of laser-structured thick-film electrodes in high-performance Li-ion batteries), project no. 519141407 (PF 392/13-1).

Data Availability Statement: The data are contained within the article.

Acknowledgments: We would like to thank our colleagues Alexandra Reif, Heino Besser, and Marek Kapitz for their strong support in laser processing, SEM analysis, and for fruitful scientific discussions.

We would also like to acknowledge scientific and technical supports from Alexandra Meyer, Ulrich Rist, and Yannic Sterzl with regard to slurry mixing and data processing. We acknowledge support from the KIT-Publication Fund of the Karlsruhe Institute of Technology.

Conflicts of Interest: The authors declare no conflicts of interest.

References

1. Kubota, K.; Dahbi, M.; Hosaka, T.; Kumakura, S.; Komaba, S. Towards K-ion and Na-ion batteries as "beyond Li-ion". *Chem. Rec.* **2018**, *18*, 459–479. [CrossRef]
2. Bashir, T.; Ismail, S.A.; Song, Y.; Irfan, R.M.; Yang, S.; Zhou, S.; Zhao, J.; Gao, L. A review of the energy storage aspects of chemical elements for lithium-ion based batteries. *Energy Mater.* **2021**, *1*, 100019. [CrossRef]
3. Masias, A. *Lithium-Ion Battery Design for Transportation*; Springer International Publishing AG: Cham, Switzerland, 2018; pp. 1–33.
4. Wood, D.L., III; Li, J.; Daniel, C. Prospects for reducing the processing cost of lithium ion batteries. *J. Power Sources* **2015**, *275*, 234–242. [CrossRef]
5. Heubner, C.; Nickol, A.; Seeba, J.; Reuber, S.; Junker, N.; Wolter, M.; Schneider, M.; Michaelis, A. Understanding thickness and porosity effects on the electrochemical performance of $LiNi_{0.6}Co_{0.2}Mn_{0.2}O_2$-based cathodes for high energy Li-ion batteries. *J. Power Sources* **2019**, *419*, 119–126. [CrossRef]
6. Park, K.-Y.; Park, J.-W.; Seong, W.M.; Yoon, K.; Hwang, T.-H.; Ko, K.-H.; Han, J.-H.; Jaedong, Y.; Kang, K. Understanding capacity fading mechanism of thick electrodes for lithium-ion rechargeable batteries. *J. Power Sources* **2020**, *468*, 228369. [CrossRef]
7. Long, J.W.; Dunn, B.; Rolison, D.R.; White, H.S. Three-dimensional battery architectures. *Chem. Rev.* **2004**, *104*, 4463–4492. [CrossRef] [PubMed]
8. Li, J.; Leu, M.C.; Panat, R.; Park, J. A hybrid three-dimensionally structured electrode for lithium-ion batteries via 3D printing. *Mater. Des.* **2017**, *119*, 417–424. [CrossRef]
9. Airoldi, L.; Anselmi-Tamburini, U.; Vigani, B.; Rossi, S.; Mustarelli, P.; Quartarone, E. Additive Manufacturing of Aqueous-Processed $LiMn_2O_4$ Thick Electrodes for High-Energy-Density Lithium-Ion Batteries. *Batter. Supercaps* **2020**, *3*, 1040–1050. [CrossRef]
10. Li, L.; Tan, H.; Yuan, X.; Ma, H.; Ma, Z.; Zhao, Y.; Zhao, J.; Wang, X.; Chen, D.; Dong, Y. Direct ink writing preparation of $LiFePO_4$/MWCNTs electrodes with high-areal Li-ion capacity. *Ceram. Int.* **2021**, *47*, 21161–21166. [CrossRef]
11. Gupta, V.; Alam, F.; Verma, P.; Kannan, A.; Kumar, S. Additive manufacturing enabled, microarchitected, hierarchically porous polylactic-acid/Lithium iron phosphate/carbon nanotube nanocomposite electrodes for high performance Li-Ion batteries. *J. Power Sources* **2021**, *494*, 229625. [CrossRef]
12. Plateau, T.P.; Pham, H.; Zhu, Y.; Leu, M.; Park, J. Enabling Ultrathick Electrodes via a Microcasting Process for High Energy and Power Density Lithium-Ion Batteries. *Adv. Energy Mater.* **2022**, *12*, 2201353. [CrossRef]
13. Keilhofer, J.; Schaffranka, L.W.F.; Wuttke, A.; Günter, F.J.; Hille, L.; Dorau, F.A.; Daub, R. Mechanical Structuring of Lithium-Ion Battery Electrodes Using an Embossing Roller. *Energy Technol.* **2023**, *11*, 2200869. [CrossRef]
14. Lu, L.L.; Lu, Y.Y.; Xiao, Z.J.; Zhang, T.W.; Zhou, F.; Ma, T.; Ni, Y.; Yao, H.B.; Yu, S.H.; Cui, Y. Wood-inspired high-performance ultrathick bulk battery electrodes. *Adv. Mater.* **2018**, *30*, 1706745. [CrossRef]
15. Huang, C.; Grant, P.S. Coral-like directional porosity lithium ion battery cathodes by ice templating. *J. Mater. Chem. A* **2018**, *6*, 14689–14699. [CrossRef]
16. Huang, C.; Dontigny, M.; Zaghib, K.; Grant, P.S. Low-tortuosity and graded lithium ion battery cathodes by ice templating. *J. Mater. Chem. A* **2019**, *7*, 21421–21431. [CrossRef]
17. Pröll, J.; Kohler, R.; Torge, M.; Bruns, M.; Przybylski, M.; Ulrich, S.; Seifert, H.; Pfleging, W. Laser-adjusted three-dimensional Li-Mn-O cathode architectures for secondary lithium-ion cells. In Proceedings of the Laser-based Micro-and Nanopackaging and Assembly VI, San Francisco, CA, USA, 24–26 January 2012; pp. 202–211.
18. Pfleging, W.; Pröll, J. A new approach for rapid electrolyte wetting in tape cast electrodes for lithium-ion batteries. *J. Mater. Chem. A* **2014**, *2*, 14918–14926. [CrossRef]
19. Habedank, J.B.; Günter, F.J.; Billot, N.; Gilles, R.; Neuwirth, T.; Reinhart, G.; Zaeh, M.F. Rapid electrolyte wetting of lithium-ion batteries containing laser structured electrodes: In situ visualization by neutron radiography. *Int. J. Adv. Manuf. Technol.* **2019**, *102*, 2769–2778. [CrossRef]
20. Berhe, M.G.; Oh, H.G.; Park, S.-K.; Mondal, M.; Lee, D. Effect of laser-induced groove morphology on the wettability and performance of Lithium-ion batteries. *Mater. Des.* **2023**, *231*, 112020. [CrossRef]
21. Park, J.; Hyeon, S.; Jeong, S.; Kim, H.-J. Performance enhancement of Li-ion battery by laser structuring of thick electrode with low porosity. *J. Ind. Eng. Chem.* **2019**, *70*, 178–185. [CrossRef]
22. Zhu, P.; Trouillet, V.; Heißler, S.; Pfleging, W. Laser structuring of high mass loaded and aqueous acid processed Li $(Ni_{0.6}Mn_{0.2}Co_{0.2})O_2$ cathodes for lithium-ion batteries. *J. Energy Storage* **2023**, *66*, 107401. [CrossRef]
23. Dunlap, N.; Sulas-Kern, D.B.; Weddle, P.J.; Usseglio-Viretta, F.; Walker, P.; Todd, P.; Boone, D.; Colclasure, A.M.; Smith, K.; de Villers, B.J.T. Laser ablation for structuring Li-ion electrodes for fast charging and its impact on material properties, rate capability, Li plating, and wetting. *J. Power Sources* **2022**, *537*, 231464. [CrossRef]

24. Hille, L.; Xu, L.; Keilhofer, J.; Stock, S.; Kriegler, J.; Zaeh, M.F. Laser structuring of graphite anodes and NMC cathodes–Proportionate influence on electrode characteristics and cell performance. *Electrochim. Acta* **2021**, *392*, 139002. [CrossRef]
25. Park, J.; Jeon, C.; Kim, W.; Bong, S.-J.; Jeong, S.; Kim, H.-J. Challenges, laser processing and electrochemical characteristics on application of ultra-thick electrode for high-energy lithium-ion battery. *J. Power Sources* **2021**, *482*, 228948. [CrossRef]
26. Tran, M.X.; Smyrek, P.; Park, J.; Pfleging, W.; Lee, J.K. Ultrafast-Laser Micro-Structuring of $LiNi_{0.8}Mn_{0.1}Co_{0.1}O_2$ Cathode for High-Rate Capability of Three-Dimensional Li-ion Batteries. *Nanomaterials* **2022**, *12*, 3897. [CrossRef]
27. Schweighofer, L.; Eschelmüller, B.; Fröhlich, K.; Pfleging, W.; Pichler, F. Modelling and Optimisation of Laser-Structured Battery Electrodes. *Nanomaterials* **2022**, *12*, 1574. [CrossRef]
28. Park, D.; Lee, D. Effect of fluence and multi-pass on groove morphology and process efficiency of laser structuring for 3D electrodes of lithium-ion batteries. *Materials* **2021**, *14*, 1283. [CrossRef]
29. Dubey, R.; Zwahlen, M.D.; Shynkarenko, Y.; Yakunin, S.; Fuerst, A.; Kovalenko, M.V.; Kravchyk, K.V. Laser patterning of high-mass-loading graphite anodes for high-performance Li-ion batteries. *Batter. Supercaps* **2021**, *4*, 464–468. [CrossRef]
30. Meyer, A.; Ball, F.; Pfleging, W. The effect of silicon grade and electrode architecture on the performance of advanced anodes for next generation lithium-ion cells. *Nanomaterials* **2021**, *11*, 3448. [CrossRef] [PubMed]
31. Tsuda, T.; Ando, N.; Matsubara, K.; Tanabe, T.; Itagaki, K.; Soma, N.; Nakamura, S.; Hayashi, N.; Gunji, T.; Ohsaka, T. Improvement of high-rate charging/discharging performance of a lithium ion battery composed of laminated $LiFePO_4$ cathodes/graphite anodes having porous electrode structures fabricated with a pico-second pulsed laser. *Electrochim. Acta* **2018**, *291*, 267–277. [CrossRef]
32. Tsuda, T.; Ishihara, Y.; Watanabe, T.; Ando, N.; Gunji, T.; Soma, N.; Nakamura, S.; Hayashi, N.; Ohsaka, T.; Matsumoto, F. An improved high-rate discharging performance of "unbalanced" $LiFePO_4$ cathodes with different $LiFePO_4$ loadings by a grid-patterned micrometer size-holed electrode structuring. *Electrochemistry* **2019**, *87*, 370–378. [CrossRef]
33. Yamada, M.; Soma, N.; Tsuta, M.; Nakamura, S.; Ando, N.; Matsumoto, F. Development of a roll-to-roll high-speed laser micro processing machine for preparing through-holed anodes and cathodes of lithium-ion batteries. *Int. J. Extrem. Manuf.* **2023**, *5*, 035004. [CrossRef]
34. Kriegler, J.; Hille, L.; Stock, S.; Kraft, L.; Hagemeister, J.; Habedank, J.B.; Jossen, A.; Zaeh, M.F. Enhanced performance and lifetime of lithium-ion batteries by laser structuring of graphite anodes. *Appl. Energy* **2021**, *303*, 117693. [CrossRef]
35. Habedank, J.B.; Endres, J.; Schmitz, P.; Zaeh, M.F.; Huber, H.P. Femtosecond laser structuring of graphite anodes for improved lithium-ion batteries: Ablation characteristics and process design. *J. Laser Appl.* **2018**, *30*, 032205. [CrossRef]
36. Hille, L.; Noecker, M.P.; Ko, B.; Kriegler, J.; Keilhofer, J.; Stock, S.; Zaeh, M.F. Integration of laser structuring into the electrode manufacturing process chain for lithium-ion batteries. *J. Power Sources* **2023**, *556*, 232478. [CrossRef]
37. Usseglio-Viretta, F.L.E.; Weddle, P.; Tremolet de Villers, B.J.; Dunlap, N.; Kern, D.; Smith, K.; Finegan, D. Optimizing Fast Charging and Wetting in Lithium-Ion Batteries with Optimal Microstructure Patterns Identified by Genetic Algorithm. *J. Electrochem. Soc.* **2023**, *170*, 120506. [CrossRef]
38. Kleefoot, M.-J.; Sandherr, J.; Sailer, M.; Nester, S.; Martan, J.; Knoblauch, V.; Kumkar, M.; Riegel, H. Investigation on the parameter dependency of the perforation process of graphite based lithium-ion battery electrodes using ultrashort laser pulses. *J. Laser Appl.* **2022**, *34*, 042003. [CrossRef]
39. Hille, L.; Kriegler, J.; Oehler, A.; Chaja, M.; Wagner, S.; Zaeh, M.F. Picosecond laser structuring of graphite anodes—Ablation characteristics and process scaling. *J. Laser Appl.* **2023**, *35*, 042054. [CrossRef]
40. Zheng, Y.; Yin, D.; Seifert, H.J.; Pfleging, W. Investigation of Fast-Charging and Degradation Processes in 3D Silicon–Graphite Anodes. *Nanomaterials* **2021**, *12*, 140. [CrossRef] [PubMed]
41. Wentker, M.; Greenwood, M.; Leker, J. A bottom-up approach to lithium-ion battery cost modeling with a focus on cathode active materials. *Energies* **2019**, *12*, 504. [CrossRef]
42. Song, Z.; Zhu, P.; Pfleging, W.; Sun, J. Electrochemical performance of thick-film $Li(Ni_{0.6}Mn_{0.2}Co_{0.2})O_2$ cathode with hierarchic structures and laser ablation. *Nanomaterials* **2021**, *11*, 2962. [CrossRef]
43. Günter, F.; Wassiliadis, N. State of the art of lithium-ion pouch cells in automotive applications: Cell teardown and characterization. *J. Electrochem. Soc.* **2022**, *169*, 030515. [CrossRef]
44. Habedank, J.B.; Kraft, L.; Rheinfeld, A.; Krezdorn, C.; Jossen, A.; Zaeh, M.F. Increasing the discharge rate capability of lithium-ion cells with laser-structured graphite anodes: Modeling and simulation. *J. Electrochem. Soc.* **2018**, *165*, A1563. [CrossRef]
45. Smyrek, P.; Bergfeldt, T.; Seifert, H.J.; Pfleging, W. Laser-induced breakdown spectroscopy for the quantitative measurement of lithium concentration profiles in structured and unstructured electrodes. *J. Mater. Chem. A* **2019**, *7*, 5656–5665. [CrossRef]
46. Pfleging, W. Recent progress in laser texturing of battery materials: A review of tuning electrochemical performances, related material development, and prospects for large-scale manufacturing. *Int. J. Extrem. Manuf.* **2020**, *3*, 012002. [CrossRef]
47. Matsumoto, F.; Yamada, M.; Tsuta, M.; Nakamura, S.; Ando, N.; Soma, N. Review of the structure and performance of through-holed anodes and cathodes prepared with a picosecond pulsed laser for lithium-ion batteries. *Int. J. Extrem. Manuf.* **2022**, *5*, 012001. [CrossRef]
48. Zheng, H.; Li, J.; Song, X.; Liu, G.; Battaglia, V.S. A comprehensive understanding of electrode thickness effects on the electrochemical performances of Li-ion battery cathodes. *Electrochim. Acta* **2012**, *71*, 258–265. [CrossRef]

49. De Meatza, I.; Urdampilleta, I.; Boyano, I.; Castrillo, I.; Landa-Medrano, I.; Sananes-Israel, S.; Eguia-Barrio, A.; Palomares, V. From Lab to Manufacturing Line: Guidelines for the Development and Upscaling of Aqueous Processed NMC622 Electrodes. *J. Electrochem. Soc.* **2023**, *170*, 010527. [CrossRef]
50. Wei, Y.; Zheng, J.; Cui, S.; Song, X.; Su, Y.; Deng, W.; Wu, Z.; Wang, X.; Wang, W.; Rao, M. Kinetics tuning of Li-ion diffusion in layered $Li(Ni_xMn_yCo_z)O_2$. *J. Am. Chem. Soc.* **2015**, *137*, 8364–8367. [CrossRef]
51. Hofmann, M.; Kapuschinski, M.; Guntow, U.; Giffin, G.A. Implications of aqueous processing for high energy density cathode materials: Part I. Ni-rich layered oxides. *J. Electrochem. Soc.* **2020**, *167*, 140512. [CrossRef]
52. Denis, Y.; Fietzek, C.; Weydanz, W.; Donoue, K.; Inoue, T.; Kurokawa, H.; Fujitani, S. Study of $LiFePO_4$ by cyclic voltammetry. *J. Electrochem. Soc.* **2007**, *154*, A253.